Optimization of Thermal-Wave Radar Thermography by Transverse Heat Flow Suppression Technique for Accurate Defect Detection of CFRP Laminates

Fei Wang, Junyan Liu, Boyuan Dong, Guobin Liu, Mingjun Chen, and Yang Wang

***Abstract*—In this present study, transverse heat flow suppression (THFS) technique was proposed to enhance the ability of thermal-wave radar thermography (TWRT) to resist lateral thermal diffusion and uneven heating. The enhanced TWRT was used to detect subsurface defects of CFRP laminates. The principle of THFS was described in details by optical flow analogy. The three dimension (3D) thermal-wave model which stimulated by the uneven linear frequency modulation (LFM) thermal flow was introduced. The thermal-wave signal was processed by several different post-processing characteristic extraction algorithms (Cross-correlation algorithm, CC, Dual-orthogonal demodulation algorithm, DOD, Fractional Fourier transform, FrFT, and Principal component analysis, PCA). The comparison between normalized DOD amplitude/phase and normalized DOD-THFS amplitude/phase was carried out. The simulation results depicted THFS can significantly improve the difference between defect location and non-defect location. Nine CFRP specimens with artificial flat-bottom holes (FBHs) were prepared for nondestructive testing and evaluation (NDT&E) by enhanced TWRT. 72 FBHs were prepared to test the probability of detection (PoD) of the enhanced TWRT. Hit/miss method was used to count defect information. The results demonstrated that the enhanced TWRT can realize the effective detection of defects (90% detection probability) with a diameter depth ratio of 5.06 under 95% confidence level. Compared with two state-of-the-art approaches, the proposed DOD-THFS phase has a better defect detection SNR.**

***Index Terms*—transverse heat flow suppression (THFS), enhanced thermal-wave radar thermography, defects, CFRP.**

I. Introduction

Carbon fiber reinforced plastics (CFRP) has the merits of lightweight, high strength, corrosion resistance, and adjustable anisotropy [1]. In recent years, with the development of fiber knitting technology, the cost of carbon fiber reinforced plastics (CFRP) material is reduced, which makes it widely application in aerospace, vehicle manufacturing and some light industry fields (UAV shell, bicycle, badminton racket, etc.). Taking Airbus A350XWB aircraft as an example, the proportion of CFRP in structural materials has reached 53% [2]. The advantages of integrated structure, automatic system installation and automatic fiber placement of carbon fiber structure parts promote the large-scale application of CFRP. However, in the process of production, processing and use, CFRP is prone to produce various types of defects, including interlayer defects, matrix cracks, and inclusion defects, which seriously affect the service performance of composite components [3]. Meanwhile, interlayer defects are the main damage forms of the defects in CFRP materials. The existence of interlayer defects greatly reduces the structural stiffness. Under the action of compression load, the structure is prone to layered expansion, which leads to the failure of the structure below its compression strength. Therefore, nondestructive testing and evaluation (NDT&E) techniques are necessarily employed to control CFRP materials' quality effectively.

At present, conventional detection methods for CFRP defects mainly include ultrasonic, acoustic emission, and X-ray, et al. Although these methods can be used to detect the defects of CFRP, they have the disadvantages of low efficiency, high cost and poor resolution [4-6]. Therefore, it is urgent to find a NDT&E technique which can achieve non-destructive, high efficiency and low-cost detection for CFRP defects.

With the improvement of infrared detector precision, active infrared thermography technique as a new NDT&E method is gradually applied to the defect's detection of composite materials [7-11]. Active infrared thermography has the merit of large detection area, non-contact, and low cost, which provides a solution for the high efficiency detection of subsurface defects of CFRP laminates. Based on the difference type of heat flow excitation signal, the active infrared thermography can be divided into pulse thermography (PT), lock-in thermography (LIT), and thermal-wave radar thermography (TWRT). PT uses short-term high-energy pulse signals as the thermal flow excitation signals [12-13]. Therefore, this method has limited detection depth. LIT technology applies a sinusoidal modulation signal as the thermal flow excitation signal [14]. However, due to the correlation between the depth of thermal wave detection and frequency, the detection efficiency of LIT is low. The excitation signal of TWRT is a linear frequency modulation (LFM) signal [15]. LFM signal has a large time-width-bandwidth product, and the application of the pulse

This work was supported by the Foundation for Innovative Research Groups of the NSFC under Grant No. 51521003, NSFC under Contract No. 61571153, No. 51173034, Postdoctoral innovative talents support program(BX2021092), China Postdoctoral Science Foundation (No. 2021M690841), Heilongjiang Postdoctoral Fund (No. LBH-Z20019), Aeronautical Science Foundation of China (No. 2020Z057077001), and Self-planned Task of State Key Laboratory of Robotics and System (HIT), the Programme of Introducing Talents of Discipline of Universities (Grant No. B07108).

F. Wang, J. Liu, B. Dong, M. Chen and Y. Wang are with School of Mechatronics Engineering, Harbin Institute of Technology, State Key Laboratory of Robotics and System (HIT), Harbin, 150001, P.R. China. G. Liu is with the 41th Institute of Sixth Academy of CASIC, Hohhot, 010010, P.R. China. Corresponding author: Junyan Liu (E-mail: ljywlj@hit.edu.cn).

compression matched filtering technology further improves the detection efficiency and detection effect of the TWRT. R. Mulaveesala first proposed to detect CFRP defects using digitized frequency modulated thermal wave imaging (DFMTWI) and frequency modulated thermal wave imaging (FMTWI) [16]. For the first time, these two techniques try to use frequency modulation signal as thermal flow excitation signal. A. Mandelis named the active thermal imaging technology with LFM as excitation signal as TWRT [17]. He applied TWRT to the detection of human early caries, and achieved good detection results [18]. J.Y. Liu has made deep researches on defect detection of CFRP laminate by TWRT [19]. In summary, TWRT has a great advantage for CFRP defect detection.

However, for all the thermal-wave imaging technologies, the lateral thermal diffusion and uneven heating greatly affect the defects detection effect. To reduce or eliminate the influence of transverse thermal diffusion and uneven heating, a more commonly used method is to select a characteristic parameter with a poor correlation with energy to detect defects, such as the LIT phase characteristic [20-21]. X. Maldague first proposed the pulse phase algorithm to extract the pulse thermal-wave signal, and the application of phase characteristic greatly reduces the influence of uneven heating [22]. R. Mulaveesala selected the CC delay time of pulse compression matched filtering algorithm as the characteristic parameter [23]. Lots of advance post-processing algorithms, such as matrix factorization techniques (semi-, convex-, and sparse-NMF), convolutional neural network, and some new time-frequency analysis methods (Fractional Fourier transform), were employed to enhance the defect recognition effect [24-27].

To further enhance the defect detection capability of TWRT for CFRP laminates, in this paper, transverse heat flow suppression (THFS) technique based on optical flow was proposed and applied to enhance the ability of TWRT to resist lateral thermal diffusion and uneven heating. This paper is arranged and structured as follows. Firstly, the principle of THFS is introduced in detail. Then, the combination of THFS and TWRT detection was described. Subsequently, the thermal-wave mathematic model which stimulated by the uneven linear frequency modulation (LFM) thermal flow was introduced in detail. Meanwhile, finite element analysis method was used to analyze theoretically the diffusion behavior of thermal-wave. Furthermore, experimental research on enhanced TWRT of simulation delamination defect of CFRP was carried out. Finally, the PoD of the enhanced TWRT was executed.

II. Transverse Heat Flow Suppression (THFS) Technique

A. Mathematical model

Transverse heat flow suppression (THFS) technique proposed in this paper is inspired by the Optical Flow (OF) [28-30]. The principle of enhanced thermal-wave radar thermography based on transverse heat flow suppression technique is shown in Fig. 1. Thermal diffusion processing can be obtained by OF, and theoretically, transverse thermal diffusion is eliminated by solving inverse thermal diffusion. Therefore, the key of this technique is how to use optical flow to describe heat flow diffusion phenomenon.

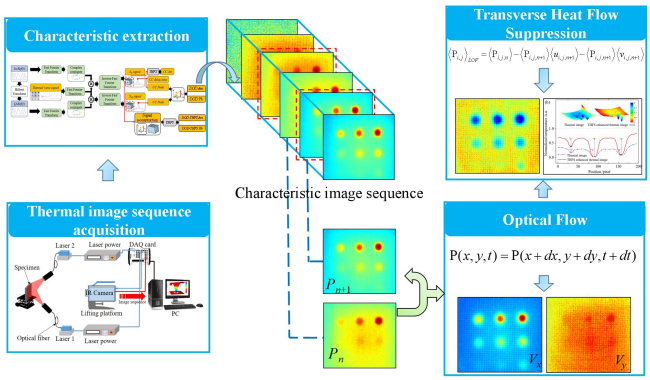

Fig. 1. The principle of enhanced thermal-wave radar thermography based on THFS technique.

THFS needs to meet the basic assumptions of the OF in the application process. The assumption is, time changes will not cause drastic changes in the target (Value of characteristic parameters), and the displacement between adjacent frames should be small. For TWRT characteristic image, a characteristic parameter pixel value $P(x, y, t)$ has moved (dx, dy) distance to the next frame within dt time. It can be described as,

$$\mathrm{P}(x,y,t)=\mathrm{P}(x+dx,y+dy,t+dt) \tag{1}$$

here, $P(x, y, t)$ is the value of the characteristic parameter pixel point (x, y) at time t, dx is x-direction displacement, dy is y-direction displacement, and dt is the time variable.

Taylor series expansion of Eq. (1) is given by,

$$\mathrm{P}(x,y,t)=\mathrm{P}(x,y,t)+\frac{\partial \mathrm{P}}{\partial x}dx+\frac{\partial \mathrm{P}}{\partial y}dy+\frac{\partial \mathrm{P}}{\partial t}dt+\zeta \tag{2}$$

here, ζ is second-order infinitesimal term, and this parameter is negligible. Combining Eq. (1) and Eq. (2), the following equation can be obtained,

$$\frac{\partial \mathrm{P}}{\partial x}u(x,y)+\frac{\partial \mathrm{P}}{\partial y}v(x,y)+\frac{\partial \mathrm{P}}{\partial t}=0 \tag{3a}$$

$$u(x,y)=\frac{dx}{dt} \tag{3b}$$

$$v(x,y)=\frac{dy}{dt} \tag{3c}$$

here, $u(x, y)$ is heat flow along the x-axis velocity vector, and $v(x, y)$ is heat flow along the y-axis velocity vector.

It can be seen from Eq. (3) that there are two unknown quantities in the equation and only one constraint equation. In this case, the exact values of $u(x, y)$ and $v(x, y)$ cannot be obtained. Additional constraints need to be added. Common constraints include gradient-based methods, matching methods, energy methods, and phase methods. Due to the simple calculation and good calculation results, the most widely used algorithm in OF field is Horn-Schunk algorithm based on gradient variation. Based on the basic constraint equation of OF, the global smoothing assumption is added to the algorithm, which assumes that the change of OF in the whole image is

smooth, that is, the motion vector of the object changes slowly. The problem of OF estimation is transformed into the following variational problem,

$$\min\iint\left\{a\left[\left(\frac{\partial u}{\partial x}\right)^2+\left(\frac{\partial u}{\partial y}\right)^2+\left(\frac{\partial v}{\partial x}\right)^2+\left(\frac{\partial v}{\partial y}\right)^2\right]+\left(\frac{\partial \mathrm{P}}{\partial x}u+\frac{\partial \mathrm{P}}{\partial y}v+\frac{\partial \mathrm{P}}{\partial t}\right)^2\right\}dxdy \quad (4)$$

here, a is smoothness weight parameter, and the variational problem shown in Eq. (4) can be solved by Euler Lagrange,

$$\left(\frac{\partial \mathrm{P}}{\partial x}\right)^2 u+\frac{\partial \mathrm{P}}{\partial x}\frac{\partial \mathrm{P}}{\partial y}v+\frac{\partial \mathrm{P}}{\partial x}\frac{\partial \mathrm{P}}{\partial t}-a\left(\frac{\partial^2 u}{\partial x^2}+\frac{\partial^2 u}{\partial y^2}\right)=0 \quad (5a)$$

$$\left(\frac{\partial \mathrm{P}}{\partial x}\right)^2 v+\frac{\partial \mathrm{P}}{\partial x}\frac{\partial \mathrm{P}}{\partial y}u+\frac{\partial \mathrm{P}}{\partial x}\frac{\partial \mathrm{P}}{\partial t}-a\left(\frac{\partial^2 v}{\partial x^2}+\frac{\partial^2 v}{\partial y^2}\right)=0 \quad (5b)$$

Eq. 5 is discretized iteratively, and Laplace operator is used to simplify it. Formula after discretization is given by,

$$\mathrm{P}_x(\mathrm{P}_x u^{(n+1)}+\mathrm{P}_y v^{(n+1)}+\mathrm{P}_t)=a\nabla^2 u \quad (6a)$$

$$\mathrm{P}_y(\mathrm{P}_x u^{(n+1)}+\mathrm{P}_y v^{(n+1)}+\mathrm{P}_t)=a\nabla^2 v \quad (6b)$$

$$\mathrm{P}_x=\frac{\partial \mathrm{P}}{\partial x},\ \mathrm{P}_y=\frac{\partial \mathrm{P}}{\partial y},\ \mathrm{P}_t=\frac{\partial \mathrm{P}}{\partial t} \quad (6c)$$

$$\nabla^2=\frac{\partial^2}{\partial x^2}+\frac{\partial^2}{\partial y^2} \quad (6d)$$

The Laplace operator is approximated as follows,

$$\nabla^2 u=u^{(n+1)}-\bar{u}^{(n)} \quad (7a)$$

$$\nabla^2 v=v^{(n+1)}-\bar{v}^{(n)} \quad (7b)$$

The average value of u and v is the average value of 8 neighborhood, and the specific expression is,

$$\bar{u}^{(n)}_{i,j,n}=\frac{1}{6}(u^{(n)}_{i-1,j,n}+u^{(n)}_{i,j+1,n}+u^{(n)}_{i+1,j,n}+u^{(n)}_{i,j-1,n})+\frac{1}{12}(u^{(n)}_{i-1,j-1,n}+u^{(n)}_{i-1,j+1,n}+u^{(n)}_{i+1,j+1,n}+u^{(n)}_{i+1,j-1,n}) \quad (8a)$$

$$\bar{v}^{(n)}_{i,j,n}=\frac{1}{6}(v^{(n)}_{i-1,j,n}+v^{(n)}_{i,j+1,n}+v^{(n)}_{i+1,j,n}+v^{(n)}_{i,j-1,n})+\frac{1}{12}(v^{(n)}_{i-1,j-1,n}+v^{(n)}_{i-1,j+1,n}+v^{(n)}_{i+1,j+1,n}+v^{(n)}_{i+1,j-1,n}) \quad (8b)$$

Two mutually decoupled equations are provided by Horn-Schunk algorithm, and then the velocity vectors in X, Y direction of OF method can be obtained,

$$u^{(n+1)}=\bar{u}^{(n)}-\frac{\mathrm{P}_x(\mathrm{P}_x\bar{u}^{(n)}+\mathrm{P}_y\bar{v}^{(n)}+\mathrm{P}_t)}{a+(\mathrm{P}_x{}^2+\mathrm{P}_x{}^2)} \quad (9a)$$

$$v^{(n+1)}=\bar{v}^{(n)}-\frac{\mathrm{P}_y(\mathrm{P}_x\bar{u}^{(n)}+\mathrm{P}_y\bar{v}^{(n)}+\mathrm{P}_t)}{a+(\mathrm{P}_x{}^2+\mathrm{P}_x{}^2)} \quad (9b)$$

$$v^{(0)}\to u^{(1)}\to v^{(2)}\to u^{(3)}\to\cdots \quad (9c)$$

The approximate expression of the first-order space-time partial derivative of the image can be obtained by the fourth-order finite difference method,

$$\mathrm{P}_x\approx\frac{1}{4}(\mathrm{P}_{i,j+1,n}-\mathrm{P}_{i,j,n}+\mathrm{P}_{i+1,j+1,n}-\mathrm{P}_{i+1,j,n}+\mathrm{P}_{i,j+1,n+1}-\mathrm{P}_{i,j,n+1}+\mathrm{P}_{i+1,j+1,n+1}-\mathrm{P}_{i+1,j,n+1}) \quad (10a)$$

$$\mathrm{P}_y\approx\frac{1}{4}(\mathrm{P}_{i+1,j,n}-\mathrm{P}_{i,j,n}+\mathrm{P}_{i+1,j+1,n}-\mathrm{P}_{i,j+1,n}+\mathrm{P}_{i+1,j,n+1}-\mathrm{P}_{i,j,n+1}+\mathrm{P}_{i+1,j+1,n+1}-\mathrm{P}_{i+1,j,n+1}) \quad (10b)$$

$$\mathrm{P}_t\approx\frac{1}{4}(\mathrm{P}_{i,j,n+1}-\mathrm{P}_{i,j,n}+\mathrm{P}_{i+1,j,n+1}-\mathrm{P}_{i+1,j,n}+\mathrm{P}_{i,j+1,n+1}-\mathrm{P}_{i,j+1,n}+\mathrm{P}_{i+1,j+1,n+1}-\mathrm{P}_{i+1,j+1,n}) \quad (10c)$$

To meet the basic assumptions of the method, the characteristic image and direction vector in the calculation are normalized. The characteristic image obtained by THFS is given by,

$$\langle\mathrm{P}_{i,j}\rangle_{THFS}=\langle\mathrm{P}_{i,j,n}\rangle-\langle\mathrm{P}_{i,j,n+1}\rangle\langle u_{i,j,n+1}\rangle-\langle\mathrm{P}_{i,j,n+1}\rangle\langle v_{i,j,n+1}\rangle \quad (11a)$$

$$\langle\mathrm{P}_{i,j,n}\rangle=\frac{\max(\mathrm{P}_{i,j,n})-\mathrm{P}_{i,j,n}}{\max(\mathrm{P}_{i,j,n})-\min(\mathrm{P}_{i,j,n})} \quad (11b)$$

$$\langle u_{i,j,n}\rangle=\frac{\max(u_{i,j,n+1})-u_{i,j,n+1}}{\max(u_{i,j,n+1})-\min(u_{i,j,n+1})} \quad (11c)$$

$$\langle v_{i,j,n}\rangle=\frac{\max(v_{i,j,n+1})-v_{i,j,n+1}}{\max(v_{i,j,n+1})-\min(v_{i,j,n+1})} \quad (11d)$$

Through the description of the above mathematical language, the principle of THFS is introduced in detail. Thermal image sequence can be obtained directly, but THFS need to process the characteristic image sequence. Therefore, several characteristic extraction algorithms are introduced to extract the characteristic of thermal wave signal. In this paper, time-frequency algorithms (Cross-correlation algorithm, CC, dual-orthogonal demodulation algorithm, DOD, and Fractional Fourier transform, FrFT) and statistical analysis approaches (Principal component analysis, PCA) are employed as the characteristic extraction algorithms. These algorithms have been detailed elsewhere [31]. Therefore, this paper will not do too much to elaborate the principle of the above algorithms. Fig. 2 presents the schematic diagram of THFS and CC/DOD coupling algorithm.

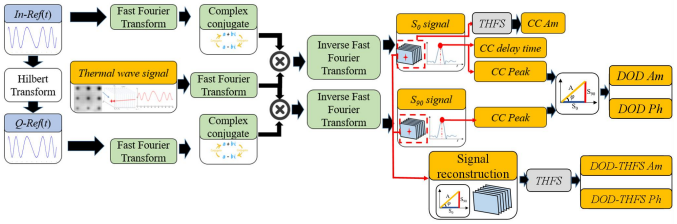

Fig. 2. Schematic diagram of THFS and CC/DOD coupling algorithm.

B. Finite Element Analysis

To verify the effectiveness of THFS in removing lateral thermal diffusion or uneven heating, finite element analysis was used to predict the heat transfer characteristic during the uneven heating. The specimen was exposed by a continuous uneven linear frequency modulation (LFM) excitation heat flow, and the expression of heat flow is given by,

$$Q(x,y,t)=Q_{LFM}(t)\times U(x,y) \quad (12a)$$

$$Q_{LFM}(t)=\frac{Q_0}{2}\left\{1+\sin\left[2\pi t(f_s+\frac{f_e-f_s}{2T_s}t)\right]\right\} \quad (12b)$$

$$U(x,y)=y^{\frac{1}{2}} \quad (12c)$$

here, $U(x, y)$ is the non-uniformity coefficient, Q_0 is the peak value of heat flow, f_s is the start frequency, f_e is the cut-off frequency, and T_s is the sweep time, respectively.

The mathematical function of 3D heat conduction in CFRP numerical model is given by,

$$\lambda_{jxx}\frac{\partial^2 T_j}{\partial x^2}+\lambda_{jyy}\frac{\partial^2 T_j}{\partial y^2}+2\lambda_{jxy}\frac{\partial^2 T_j}{\partial x\partial y}+\lambda_{jzz}\frac{\partial^2 T_j}{\partial z^2}=\rho c\frac{\partial T_j}{\partial t}\quad j=1,2,3... \tag{13}$$

here, T_j is the temperature distribution of layer j, and j is the number of layers. Only the heated surface has the convection heat transfer and radiation heat transfer, and assume other surfaces are heat insulation. The initial condition and the boundary conditions are as follows,

$$T(x,y,z,t)\big|_{t=0}=T_{am} \tag{14a}$$

$$-\lambda_1\frac{\partial T}{\partial z}\bigg|_{z=0}=Q(t)+h[T_{\text{am}}-T(x,y,0,t)]+\varepsilon\sigma_{SB}[T_{am}{}^4-T(x,y,0,t)^4] \tag{14b}$$

$$-\lambda_j\frac{\partial T_j(x,y,z,t)}{\partial z}\bigg|_{(x,y,z)\in\Omega_2}=h[T_{\text{am}}-T_j(x,y,z,t)]+\varepsilon\sigma_{SB}[T_{am}{}^4-T_j(x,y,z,t)^4] \tag{14c}$$

$$T_j(x,y,z,t)\big|_{z=jL}=T_{j+1}(x,y,z,t)\big|_{z=jL} \tag{14d}$$

$$-\lambda_j\frac{\partial T_j(x,y,z,t)}{\partial z}\bigg|_{z=jL}=-\lambda_{j+1}\frac{\partial T_{j+1}(x,y,z,t)}{\partial z}\bigg|_{z=jL}\quad j=1,2,3...N \tag{14e}$$

here, T_{am} is the ambient temperature, h is the convection heat transfer coefficient, ε is surface emissivity, and σ_{SB} is Stefan-Boltzmann constant, separately.

The relationship between the LFM excited heat flow and the thermal-wave signal (temperature signal) is established using the above mathematical model. Because the mathematical model is more complicated, it needs to be solved with the help of finite element method (FEM). In this paper, the used FEM simulation environment is the software of COMSOL Multiphysics 5.2. The geometry structure of numerical model and finite element mesh are shown in Fig. 3.

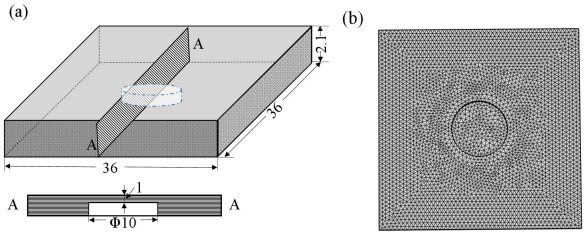

Fig. 3. (a) Geometry of simulated specimen. (b) Finite element mesh.

The thermal properties parameters of numerical model adopt the T300 CFRP laminates parameters. The parallel thermal conductivity $k_{/\!/}$ is 4.18W/(m·℃), the vertical thermal conductivity $k_{\perp}$ is 0.71W/(m·℃), the density ρ is 1760kg/m^3, and the specific heat capacity c is 795.12J/(kg·℃), respectively. The model contained seven layers fiber layup (the thickness of layer is 0.3mm), and the carbon fiber layering angles are [0° ,45° ,90° ,0° ,90° ,45° ,0°]. In this case of study, the initial frequency f_s, the end frequency f_e, the sweep time T_s, and the peak power density Q_0 of LFM excitation thermal flow were set to 0.05Hz, 0.10Hz, 40s, and 1000W/m^2, respectively. f_s-f_e-T_s-Q_0 is employed to express the LFM excitation parameters for simplification.

The thermal flow peak power density distribution is shown in Fig. 4(a). Based on the two selected thermal images, the motion vectors in X and Y directions can be obtained by THFS, and the distribution of thermal flow field is obtained by the two thermal images of the 10$^{\text{th}}$s and 11$^{\text{th}}$s, which shown in Fig. 4(b). The direction of heat diffusion can be seen clearly from the heat flow field. Meanwhile, the phenomenon of rapid drop of heat flow gradient appears at the defect location. Generally speaking, defect characteristics are not very obvious, at the same time, when the defect scale is small, the defect characteristics may be completely covered by uneven heating (transverse heat diffusion of heat flow). Because the numerical model used is a seven-layer CFRP laminates parameter, the gradient direction of the thermal decline is not completely along the Y axis, but in the direction of approximately 45°.

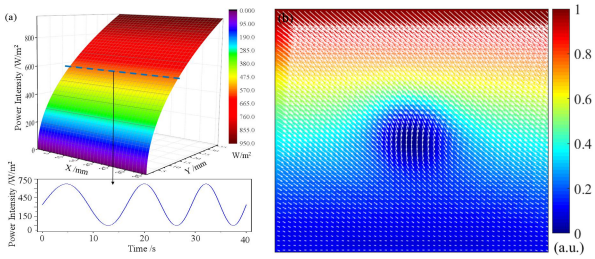

Fig. 4. (a) Thermal flow peak power density distribution; (b) Heat flow direction vector.

To facilitate the comparison of THFS enhanced TWRT with the traditional TWRT, all characteristic images are normalized. Fig. 5 depicts the normalized DOD amplitude/phase images and normalized DOD-THFS amplitude/phase images.

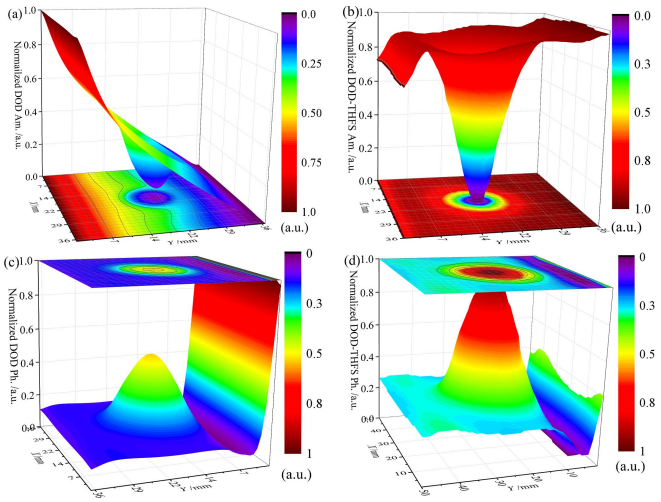

Fig. 5. Impact of THFS on the normalized DOD amplitude/phase. (a) Normalized DOD amplitude; (b) Normalized DOD-THFS amplitude; (c) Normalized DOD phase; (d) Normalized DOD-THFS phase.

It can be seen from Fig. 5, DOD amplitude is seriously affected by uneven heating or transverse thermal diffusion, while the DOD phase is less affected by it, but there is still a large characteristic mutation in the edge position. Because the normalized value range of edge position completely covers the defect value range, the edge position noise cannot be filtered out during image processing, and it is very prone to false defect determination. The effect of heating unevenness on the DOD amplitude is significantly reduced or even completely disappeared after characteristic reconstruction by THFS.

Meanwhile, the difference between the defect location and the non-defect location is more obvious after characteristic reconstruction by THFS. The difference between the defect position and the non-defect position in the original DOD amplitude image and the phase image are 0.3 and 0.4, respectively, while the difference between the defect position and the non-defect position in the DOD-THFS amplitude and phase images are 0.8 and 0.7, respectively. The defect diameter was calculated by the half height amplitude method. The defect diameter detect by original DOD amplitude/phase were 11.5 mm and 10.6 mm, respectively. The defect diameters obtained by DOD-THFS amplitude/phase were 10.5 mm and 10.4 mm, respectively.

From the above simulation experiments, THFS can significantly reduce or even eliminate the influence of uneven heating or transverse thermal diffusion on the characteristic image. Meanwhile, THFS can expand the characteristic value difference between the defect location and non-defect location, which is helpful for defect identification and judgment to a certain extent.

III. Materials And Methods

A. Specimen

Nine CFRP laminates are prepared in this present study, and labeled #ES1~ES9, respectively. #ES1 is employed to verify the effectiveness of THFS, and #ES2~ES9 are used to test PoD of enhanced TWRT based on THFS. #ES1 is T300 type CFRP, and its laying direction is [0°,45°,-45°,90°] staggered laying. The geometry size of #ES1 is 100 mm×95mm×10mm (Length× Width× Thickness). 9 artificial flat-bottomed holes (FBHs) are used to simulate delamination defect. Fig. 6 shows the optical image and the geometry structure diagram of #ES1 CFRP laminates specimen.

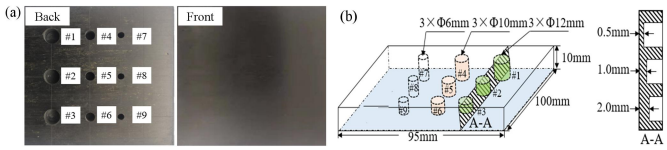

Fig. 6. (a) The optical image; (b) Geometry structure diagram of CFRP #ES1 specimen.

Fig. 7 shows the optical image and the defect diameter-depth ratio *r* vs FBH number distribution of #ES2~#ES9 specimens.

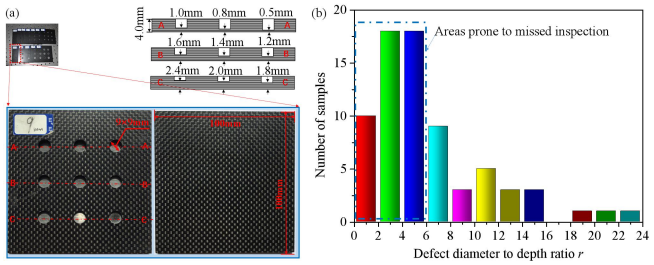

Fig. 7. Defect size of #ES2~#ES9. (a) The optical image; (b) Defect diameter-depth ratio *r* vs FBH number distribution.

The size of #ES2~#ES9 are all 100mm×100mm× 4mm. Each specimen has 9 artificial FBHs with the same diameter but different depth. The defect diameters of #ES2~#ES9 are 2mm, 3mm, 5mm, 6mm, 7mm, 9mm, 10mm, and 11mm, respectively, and the depths of 9 FBHs are from 0.5mm to 2.4mm.

B. Experimental setup

Fig. 8 depicts the schematic diagram of TWRT. Two continuous-wave 808nm near-infrared lasers (JENOTIK, Germany, the maximum power of a single laser is 50W) are used as the external excitation thermal source. A mid-infrared camera (FLIR SC7000, 320×256-pixel active elements, spectral range of 3.6μm-5.1μm, and the frame rate is 100Hz for full window size) is employed to capture the infrared thermal image sequence. A signal generation/acquisition device (National instrument, NI-6229) is controlled by PC to generate the modulation signal, and then control the laser power to change according to the modulation law. To maintain an average optical intensity for reducing heating unevenness, an appropriate laser beam homogenizer was connected to the optical fiber. This homogenizer contains three components, namely engineered diffuser, casing, and collimator, respectively. A system control software which designed under LabVIEW environment is used to control the NI-6229 and the infrared camera.

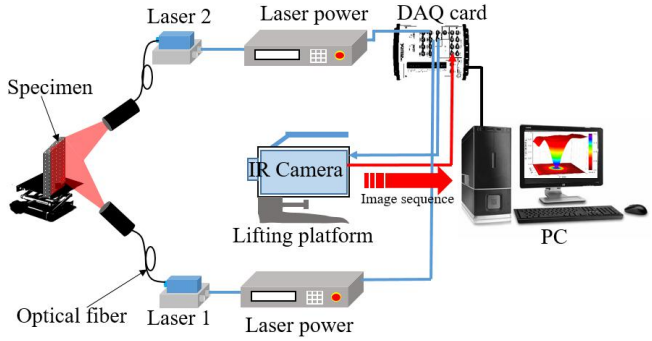

Fig. 8. The schematic diagram of TWRT.

IV. Experimental Results and Discussion

The #ES1 specimen was excited by the LFM thermal flow. Based on the geometric characteristics of defects, the modulation parameter of the excitation signal was 0.05Hz-0.10Hz-40s-1000W/m^2, and the framerate of infrared camera is 50Hz. In the actual test process, the uneven heating can be avoided as much as possible by the engineering diffusers and adjusting the position between the specimen and the excitation light source. Therefore, in the actual test process, it is impossible to have the seriously uneven thermal loading form in the simulation experiment. Fig. 9(a) shows the normalized 2s thermal image. From Fig. 9(a), the overall heat flow vector direction is from the top left to the bottom right, and the displacement vector of each pixel is small, which means that the heating uneven influence is small and the heat flow diffusion rate is small. Fig. 9(b) demonstrates the results of the normalized 2s thermal image and the comparison analysis of the thermal image sequence after THFS procession. The selected comparison positions are the peak positions of the right side #1, #2 and #3 simulated defects. From the contour curve, the defect/non-defect difference of #1~#3 defect characteristics in the original characteristic image are 0.12, 0.29 and 0.20,

respectively, while the defect/non-defect difference of defect characteristics in the image which processed by THFS technique are 0.32, 0.68 and 0.57, respectively. Moreover, THFS can make the contrast of defect position and non-defect position more obvious.

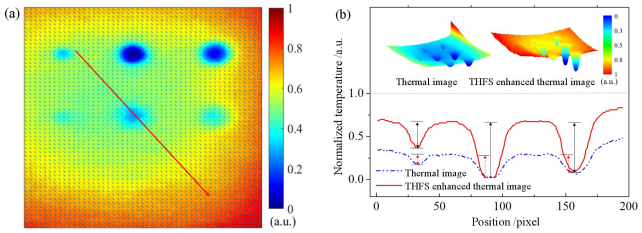

Fig. 9. (a) Normalized 2s thermal image. (b) Comparative analysis of thermal image and thermal image-THFS.

Fig. 10 presents the comparative analysis of the characteristic images and the characteristic images after THFS processing. Among them, the selected position of the comparison curve is the peak position of #1, #2 and #3 defects as shown in Fig. 10(a). It can be seen from Fig. 10, the defect detection contrast of the characteristic image processed by THFS has been improved, while for the characteristic image based on energy, such as DOD amplitude, CC amplitude and PCA characteristic, the improvement is more obvious. For PCA characteristic images, the contrast of #1~ #3 defect characteristics in PCA 1st principal component are 0.11, 0.24 and 0.24, respectively. While the contrast of defect characteristics in the PCA-THFS are 0.32, 0.77 and 0.81, respectively, and the contrast of defect characteristics is increased by more than three times. At the same time, from the normalized DOD-THFS characteristic and CC-THFS characteristic, it can be seen the curvature of the image is reduced at the non-defect position. Meanwhile, according to the defect contour curve, the waist diameter of the defect is reduced. The sampling points in non-defect area were fitted linearly, and the uneven heating was evaluated by the angle between the fitting curve and x-axis [shown in Fig. 10(b)]. After THFS processing, the angle becomes smaller. The experimental results demonstrate that THFS can suppress noise to a certain extent and control the effect of transverse thermal diffusion and uneven heating.

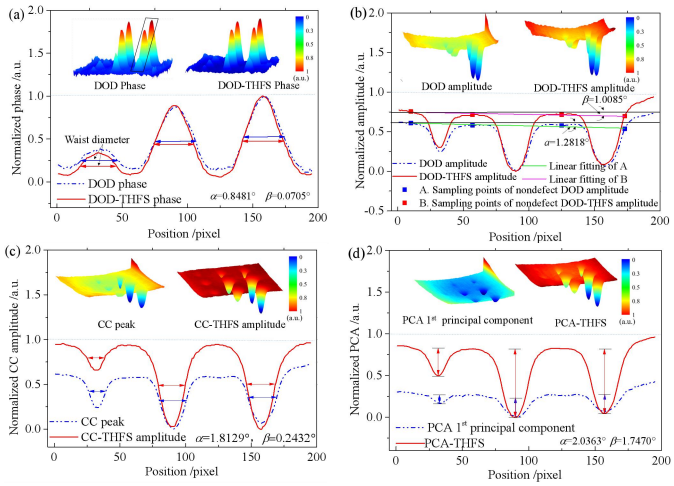

Fig. 10. Comparative analysis of characteristic images and characteristic images processed by THFS. (a) Normalized DOD phase; (b) Normalized DOD amplitude; (c) Normalized CC amplitude; (d) Normalized PCA.

It is necessary to clarify the influence of different feature extraction algorithms and defect size on the thermal wave radar signal, and the results are shown in Fig. 11. Here we define the concept of signal-to-noise ratio (*SNR*). The defect area is the inscribed square of actual defect diameter, and the non-defect areas are four squares with fixed size (12mm×12mm) in non-defect area.

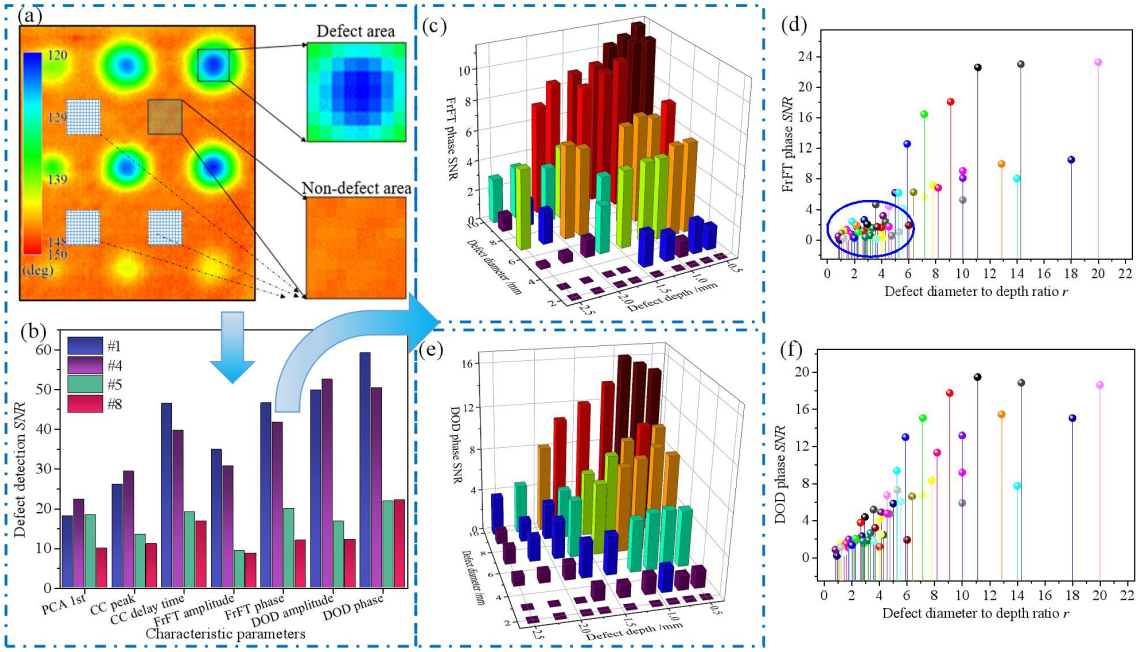

Fig. 11. The influence of different feature extraction algorithms and defect size on the thermal wave radar signal. (a) Definition of defect area and non-defect area. (b) Defect detection *SNR* in different characteristic parameters. (c) FrFT phase *SNR* vs. defect diameter and depth. (d) FrFT phase *SNR* vs. defect diameter to depth ratio *r*. (e) DOD phase *SNR* vs. defect diameter and depth. (d) DOD phase *SNR* vs. defect diameter to depth ratio *r*.

$$SNR = \frac{\Delta_{dc}}{\sigma_{nd}} \tag{15a}$$

$$\Delta_{dc} = \left| \hat{C}_{defect} - \hat{C}_{nondefect} \right| \tag{15b}$$

here, $\hat{C}_{defect}$ and $\hat{C}_{nondefect}$ are the average value of characteristic value of the defect area and non-defect area [see Fig. 11(a)], and σ_{nd} is the standard deviation of non-defect area.

The FBHs #1, #4, #5, and #8 of #ES1 detection *SNR* in different characteristic parameters are depicted in Fig. 11(b). DOD and FrFT can detect defects with high *SNR*. The #ES2, #ES3, #ES4, #ES6, #ES7, #ES8 were employed to investigate the influence of defect size, and the results are shown in Fig.11(c)~(f). With the decrease of defect depth and the increase of defect diameter, the *SNR* of DOD and FrFT phase increases gradually. From Fig. 11(d) and Fig. 11(f), when the defect diameter depth ratio *r* is less than 5, the detection *SNR* is less than 6. The DOD phase results is better than FrFT phase results. Therefore, the original DOD phase feature image sequence of #ES1 was employed to verify the effect of THFS on suppressing the transverse thermal diffusion of heat flow. DOD phase and DOD-THFS phase undergo the processes of local neighborhood statistical enhancement, median filter, image segmentation (Local threshold segmentation), morphological processing, and connected domain labeling, then, defects and non-defect positions are expressed in the binary form. Fig. 12 describes the above process.

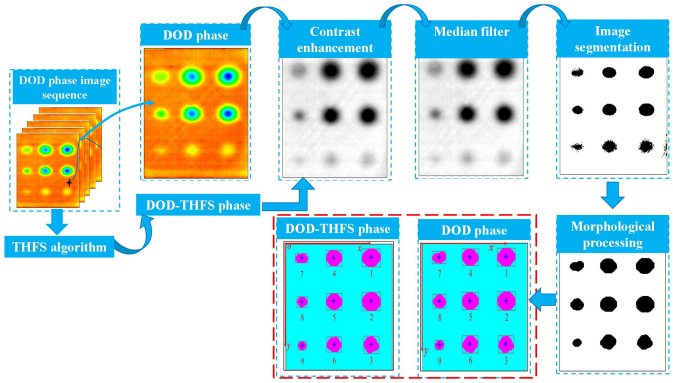

Fig. 12. Defect marking and identification.

Based on the result of connected domain marking, the inscribed circle of the marked rectangle is taken as the defect diameter, and the detection results of defect diameter by DOD and DOD-THFS phase is shown in Tab. 1.

Tab. 1. The detection results of defect diameter by DOD and DOD-THFS phase

Defect number	Actual diameter /mm	DOD phase Detect diameter/mm	error	DOD-THFS Detect diameter /mm	error
#1	12	12.47	3.91%	12.04	0.33%
#2	12	12.47	3.91%	12.47	3.91%
#3	12	11.18	6.83%	11.18	6.83%
#4	10	10.75	7.50%	10.32	3.20%
#5	10	11.18	11.80%	10.75	7.50%
#6	10	10.75	7.50%	9.89	1.10%
#7	6	6.45	7.50%	6.02	0.33%
#8	6	6.88	14.70%	6.02	0.33%
#9	6	6.02	0.30%	6.45	7.50%

The DOD-THFS detection error of each defect is within 7.50%, which is almost twice the detection error without THFS processing.

To test the detection capability of THFS enhanced TWRT, probability of detection (PoD) analysis were carried out. #ES2~#ES9 were selected for PoD analysis. Fig. 7 presents the size distribution of simulated defects, and the total number of defects is 72, which meets the minimum requirements of PoD analysis on the number of samples (≥60). The defects' optical image and the number of diameter-depth ratio *r* distribution are depicted in Fig. 7(b). According to Fig. 7(b), it can be seen the selected defect diameter-depth ratio *r* basically traverses the analysis domain of the detection method. Based on results which shown in Fig. 11, there are more defect samples distributed in the easily missed detection areas (r<5), therefore, more FBH's diameter-depth ratio *r* are distributed between 2 and 6 [see Fig. 7(b)]. In conclusion, the selected PoD analysis simulated defect samples meet the basic requirements of statistical analysis. The modulation parameters of LFM excitation signal are 0.02Hz-0.1Hz-50s-4000W/m^2. Based on the previous simulation and test analysis, the DOD-THFS phase, CC-THFS amplitude and FrFT-THFS phase have better detection effect. Therefore, DOD-THFS phase, CC-THFS amplitude and FrFT-THFS phase were selected for PoD analysis. This paper uses hit/miss method to analyze PoD of enhanced TWRT. The hit/miss method uses binary data 0 and 1 to establish the potential mathematical relationship between PoD and defect size (diameter-depth ratio *r*), while 0 means the defect is not recognized (miss), and 1 denotes the defect is recognized (hit). The link function determines the mean structure of the generalized linear model, and the selected link function used for PoD analysis is logit.

$$\text{logit link } POD(r) = \frac{\exp(f(r))}{1+\exp(f(r))} \tag{16a}$$

$$f(r) = \alpha_0 + \alpha_1 \log(r) \tag{16b}$$

here, $f(r)$ is the generalized linear model function, and α_0 and α_1 are unknown variables, respectively.

Fig. 13 illustrates the PoD analysis results of DOD-THFS phase, CC-THFS amplitude and FrFT-THFS phase by the enhanced TWRT. After PoD analysis, three more important detection indexes can be obtained, which are r_{50}, r_{90} and $r_{90/95}$. The significance of these three parameters are: detection probability of 50%, detection probability of 90% and detection probability of 90% at 95% confidence level. In the application process of various nondestructive testing methods, r_{90} is generally regarded as an important index of detection and analysis, but the value is small, which means that the detection method can detect even smaller defects, that is, the stronger the detection ability. However, in practical application, $r_{90/95}$ is generally used as the main index to evaluate and measure the detection ability of a nondestructive testing method to eliminate the influence of a series of uncertain factors such as detection environment and equipment accuracy on PoD analysis results.

It can be seen from Fig. 13, with the increase of diameter-depth ratio *r* of defects, the PoD detected gradually increases. When the DOD-THFS phase characteristic is used for defect detection, its stable diameter-depth ratio *r* of defect

detection $r_{90/95}$ is 5.321, and when it is less than this value, it is easy to miss detection or misjudge. For CC-THFS amplitude, its stable diameter-depth ratio r of defect detection $r_{90/95}$ is 5.056. For FrFT-THFS phase, its stable diameter-depth ratio r of defect detection $r_{90/95}$ is 6.089. It also shows that the CC-THFS amplitude characteristic based on energy characteristic is better than DOD-THFS and FrFT-THFS phase characteristic.

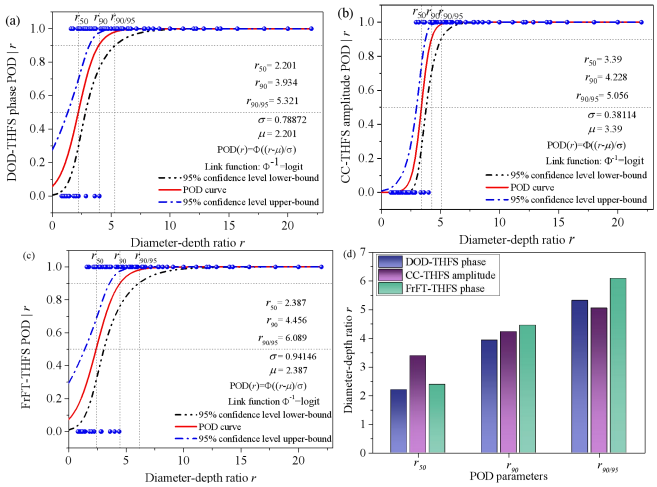

Fig. 13. POD analysis of (a) DOD-THFS phase, (b) CC-THFS amplitude and (c) FrFT-THFS phase detection; (d) POD comparison in different parameters.

The result of comparative experimental analysis in different feature extraction algorithms is shown in Fig. 14. Here, the selected state-of-the-art approaches are sparse principal component analysis (Sparse-PCA) and non-negative matrix factorization (NMF) using gradient descent (GD) [26,32]. Sparse-PCA improves the efficiency of operation, and changes the feature value of non-defect position to 0. From Fig. 14, Sparse-PCA has a good noise suppression effect, but the defects with small diameter-depth ratio r cannot be identified. NMF-GD has poor noise suppression ability, whereas it has strong ability to identify small defects. Compared with the above two state-of-the-art approaches, the proposed DOD-THFS phase has a better defect detection *SNR*.

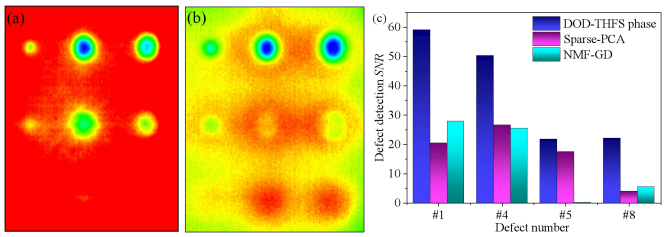

Fig. 14. Comparative experimental analysis of multi-feature extraction algorithms. (a) Sparse PCA, (b) NMF-GD and (c) defect detection *SNR* comparison.

V. Conclusions

Transverse heat flow suppression (THFS) technique was applied to enhance the ability of thermal wave radar imaging (TWRT) to resist lateral thermal diffusion and uneven heating. Firstly, the principle of THFS was presented clearly. The thermal-wave mathematic model which stimulated by the uneven linear frequency modulation (LFM) thermal flow was introduced in detail. To effectively detect defects, the thermal-wave image sequence was processed by several different post-processing characteristic extraction algorithms (Cross-correlation algorithm, CC, dual-orthogonal demodulation algorithm, DOD, Fractional Fourier transform, FrFT, and Principal component analysis, PCA). The comparison between normalized DOD amplitude/phase and normalized DOD-THFS amplitude/phase was carried out. The simulation results depicted THFS can significantly reduce the effect of lateral thermal diffusion, and improve the difference between defect location and non-defect location. The CFRP specimen with artificial flat-bottom holes (FBHs) are prepared for nondestructive testing and evaluation (NDT&E) by enhanced TWRT. The results illustrated the correctness of simulation analysis. 72 FBHs were prepared to probe the probability of detection (PoD) of the enhanced TWRT. The experimental results demonstrated that the enhanced TWRT can realize the effective detection of defects with a diameter depth ratio of 5.056 under 95% confidence level. Compared with two state-of-the-art approaches (sparse PCA and NMF-GD), the proposed DOD-THFS phase has a better defect detection *SNR*.

References

[1] T. Yokozeki, Y. Iwahori, S. Ishiwata and K. Enomoto, “Mechanical properties of CFRP laminates manufactured from unidirectional prepregs using cscnt-dispersed epoxy,” *Compos. Part A-APPL S*, vol. 38, no. 10, pp. 2121-2130, 2007.

[2] J. Haag, T. Mertens, L. Kotte and S. Kaskel, "Investigation on atmospheric plasma surface treatment for structural bonding on titanium and CFRP," *2015 IEEE International Conference on Plasma Sciences (ICOPS)*, Antalya, pp. 1-1, 2015.

[3] J. Tashan and R. Al-mahaidi, "Investigation of the parameters that influence the accuracy of bond defect detection in CFRP bonded specimens using IR thermography," *Compo. Struct.*, vol. 94, no. 2, pp. 519-531, 2012.

[4] G. Andria, F. Attivissimo, A. M. L. Lanzolla and M. Savino, "A Suitable Threshold for Speckle Reduction in Ultrasound Images," *IEEE T. Instrum. Meas.*, vol. 62, no. 8, pp. 2270-2279, Aug. 2013

[5] C. Martins, P. Aguiar, A. Frech and E. C. Bianchi, "Tool Condition Monitoring of Single-Point Dresser Using Acoustic Emission and Neural Networks Models," *IEEE T. Instrum. Meas.*, vol. 63, no. 3, pp. 667-679, March 2014

[6] C. E. Wood, N. O'Brien, A. Denysov and, T. Blumensath, "Computed laminography of CFRP using an x-ray cone-beam and robotic sample manipulator systems," *IEEE T. Nucl. Sci.*, vol. 63, no. 3, pp. 655-663, 2019.

[7] R. Usamentiaga, J. Molleda, D. F. Garcia, J. C. Granda and J. L. Rendueles, "Temperature Measurement of Molten Pig Iron With Slag Characterization and Detection Using Infrared Computer Vision," in *IEEE T. Instrum. Meas.*, vol. 61, no. 5, pp. 1149-1159, May 2012.

[8] H. Zhang, S. Sfarra, F. Sarasini, C.I. Castanedo, S. Perilli, H. Fernandes, Y.X. Duan, J. Peeters, N.P. Avdelidis, and X. Maldague, “Optical and mechanical excitation thermography for impact response in basalt-carbon hybrid fiber-reinforced composite laminates,” *IEEE T. Ind. Inform.*, vol. 14, no. 2, pp. 514-522, 2017.

[9] F. Wang, J.Y. Liu, J.H. Yang, M. Oliullah, X.C. Wang, and Y. Wang, “High-frequency heterodyne lock-in thermography (HeLIT): a highly sensitive method to detect early caries,” *Appl. Phys. Lett.*, vol. 109, no. 14, pp. 141904, 2016.

[10] Y. He and R. Yang, "Eddy Current Volume Heating Thermography and Phase Analysis for Imaging Characterization of Interface Delamination in CFRP," *IEEE T. Ind. Inform.*, vol. 11, no. 6, pp. 1287-1297, 2015.

[11] R. Yang, Y. He, A. Mandelis, N. Wang, X. Wu and S. Huang, "Induction Infrared Thermography and Thermal-Wave-Radar Analysis for Imaging

Inspection and Diagnosis of Blade Composites," *IEEE T. Ind. Inform.*, vol. 14, no. 12, pp. 5637-5647, 2018.

[12] S.D. Holland, B. Schiefelbein, "Model-based Inversion for Pulse Thermography," *Exp. Mech.*, vol. 59, no. 5, pp. 413–426, 2019.

[13] Q.J. Tang, J.Y. Liu, Y. Wang, and L. Qin, "Inspection on sic coated carbon–carbon composite with subsurface defects using pulsed thermography," *Infrared Phys. Techn.*, vol. 60, pp. 183–189, 2013.

[14] K. Chatterjee and S. Tuli, "Image Enhancement in Transient Lock-In Thermography through Time Series Reconstruction and Spatial Slope Correction," *IEEE T. Instrum. Meas.,* vol. 61, no. 4, pp. 1079-1089, 2012.

[15] J.L. Gong, J.Y. Liu, L. Qin, and Y. Wang, "Investigation of Carbon fiber reinforced polymer (CFRP) sheet with subsurface defects inspection using Thermal-wave radar imaging (TWRI) based on the Multi-Transform technique, " *NDT&E Int.*, vol. 62, no. 2, pp. 130-136, 2014.

[16] R. Mulaveesala and S. Tuli, "Theory of frequency modulated thermal wave imaging for nondestructive subsurface defect detection," *Appl. Phys. Lett.*, vol. 89, no. 19, pp.191913-1-191913-3, 2006.

[17] N. Tabatabaei and A. Mandelis, "Thermal-wave radar: a novel subsurface imaging modality with extended depth-resolution dynamic range," *Rev. Sci. Instrum.*, vol. 80, no. 3, pp. 034902, 2009.

[18] N. Tabatabaei and A. Mandelis, "Thermal Coherence Tomography: Depth-Resolved Imaging in Parabolic Diffusion-Wave Fields Using the Thermal-Wave Radar," *Int. J. Thermophys.*, vol. 33, pp. 1989-1995, 2012.

[19] F. Wang, Y.H. Wang, J.Y. Liu, Y. Wang, "Optical excitation fractional Fourier transform (FrFT) based enhanced thermal-wave radar imaging (TWRI) ," *Opt. Express*, vol. 26, no. 17, pp. 21403-21417, 2018.

[20] G. Busse, D. Wu, W. Karpen, "Thermal-wave imaging with phase sensitive modulated thermography," *J. Appl. Phys.*, vol. 71, no. 8, pp.3962–3965, 1992.

[21] O. Breitenstein, M. Langenkamp, O. Lang, and A. Schirrmacher, "Shunts due to laser scribing of solar cells evaluated by highly sensitive lock-in thermography," *Sol. Energ. Mat. Sol. C.*, vol. 65, pp. 55–62, 2001.

[22] X. Maldague, and S. Marinetti, "Pulsed phase infrared thermography," *J. Appl. Phys.*, vol. 79, no. 5, pp. 2694-2698, 1996.

[23] V. Arora, R. Mulaveesala, and, P. Bison, "Effect of spectral reshaping on frequency modulated thermal wave imaging for non-destructive testing and evaluation of steel material," *J. Nondest. Eval.*, vol. 35, no. 1, pp. 1-7, 2016.

[24] J. Wu, S. Sfarra and Y. Yao, "Sparse Principal Component Thermography for Subsurface Defect Detection in Composite Products," *IEEE T. Ind. Inform.*, vol. 14, no. 12, pp. 5594-5600, 2018.

[25] Chunli Fan, Fengrui Sun and Li Yang, "A general quantitative identification algorithm of subsurface defect for infrared thermography," 2005 Joint 30th International Conference on Infrared and Millimeter Waves and 13th International Conference on Terahertz Electronics, Williamsburg, VA, USA, vol. 2, pp. 341-342 2005.

[26] B. Yousefi, S. Sfarra, F. Sarasini, C.I. Castanedo, and XPV Maldague, "Low-rank sparse principal component thermography (sparse-PCT): Comparative assessment on detection of subsurface defects," *Infra Phys. Technol.*, vol. 98, pp. 278-284, 2019.

[27] F. Wang, J. Liu, B. Dong, J. Gong, W. Peng, Y. Wang, M. Chen, G. Liu. "Blind image separation for the debonding defects recognition of the solid propellant rocket motor cladding layer using pulse thermography," *Measurement*, vol.174, pp. 108997, 2021.

[28] F. Barranco, J. Diaz, B. Pino and E. Ros, "Real-Time Visual Saliency Architecture for FPGA With Top-Down Attention Modulation," *IEEE T. Ind. Inform.*, vol. 10, no. 3, pp. 1726-1735, 2014.

[29] L. Cheng and G. Y. Tian, "Transient Thermal Behavior of Eddy-Current Pulsed Thermography for Nondestructive Evaluation of Composites," *IEEE T. Instrum. Meas.*, vol. 62, no. 5, pp. 1215-1222, 2013.

[30] Y. Wang et al., "Thermal Pattern Contrast Diagnostic of Microcracks With Induction Thermography for Aircraft Braking Components," *IEEE T. Ind. Inform.*, vol. 14, no. 12, pp. 5563-5574, Dec. 2018,

[31] F. Wang, Y. Wang, J. Liu, and Y. Wang. The Feature Recognition of CFRP Subsurface Defects Using Low Energy Chirp-Pulsed Radar Thermography," *IEEE T. Ind. Inform.*, vol. 16, no. 8, pp. 5160-5168, 2020.

[32] B. Yousefi, C.I. Castanedo and X.P.V. Maldague, "Measuring Heterogeneous Thermal Patterns in Infrared-Based Diagnostic Systems Using Sparse Low-Rank Matrix Approximation: Comparative Study," *IEEE T. Instrum. Meas.*, vol. 70, pp. 1-9, 2021

Fei Wang is currently a lecturer in School of Mechatronics Engineering, Harbin Institute of Technology (since 2020). He received the B.Sc. degree in Mechanical Design and Manufacturing from Ludong University, Yantai, China in 2012. He received the M.Sc. and Ph.D. degree in Manufacturing Engineering of Aerospace Vehicle from Harbin Institute of Technology, Harbin, China in 2015 and 2020, respectively. His research interests include non-destructive evaluation, photothermal imaging, and infrared thermography.

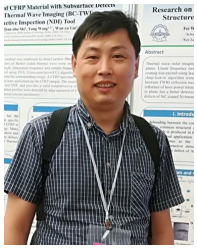

Junyan Liu received the B.Sc. and M.Sc. degrees in Mechanical Manufacturing Engineering from Jiamusi University, Jiamusi, China in 2000 and 2002, and the Ph.D. degree in Mechanical Manufacturing Engineering from Harbin Institute of Technology, Harbin, China in 2005, respectively. He is currently a full professor in School of Mechatronics Engineering, Harbin Institute of Technology (since 2006). His research interests concern photothermal science and technology, photo electronic diagnosis to semiconductor, and Mechanical hybrid machining.

Boyuan Dong is currently pursuing the M.Sc. degree in Manufacturing Engineering of Aerospace Vehicle with Harbin Institute of Technology (HIT), Harbin, China. His research interests include image processing, infrared thermography, and circuit design.

Guobin Liu is currently a researcher in the 41th Institute of Sixth Academy of *CASIC*, Hohhot, China. His research interests include image processing, infrared thermography, and circuit design.

Mingjun Chen is currently a full professor in the School of Mechatronics Engineering, Harbin Institute of Technology. His research interests are non-destructive evaluation, and micro/nanomanufacturing technology.

Yang Wang is a full professor in the School of Mechatronics Engineering, Harbin Institute of Technology (since 1982, head of the Dept. 2008-2018). He has trained over 60 graduate students (M.Sc. and Ph.D.) and more than 200 publications. He received the B.S., M.S., and Ph.D. degrees in Mechanical Manufacturing Engineering from Harbin Institute of Technology, Harbin, China in 1982, 1988 and 1999, respectively. His research interests include non-destructive testing and evaluation (NDT&E) technique, and advanced laser manufacturing technology.